AGU ADVANCING EARTH AND SPACE SCIENCES

Geophysical Research Letters®

Key Points:

- Plasma lifting during the storm caused midlatitude displacements of ionospheric peak height by as much as 300 km over the course of 1 hour
- Sporadic-E is observed at the sub-auroral convective boundary edge of the storm-enhanced density with strong plasma drift shears present
- Severe depletion of electron density at mid and high latitudes significantly reduced the impact of subsequent geomagnetic activity on GNSS

Correspondence to:
D. R. Themens,
d.r.themens@bham.ac.uk

The High Latitude Ionospheric Response to the Major May 2024 Geomagnetic Storm: A Synoptic View

David R. Themens[1,2] [ID], Sean Elvidge[1] [ID], Anthony McCaffrey[2] [ID], P. T. Jayachandran[2] [ID], Anthea Coster[3] [ID], Roger H. Varney[4] [ID], Ivan Galkin[5], Lindsay V. Goodwin[6] [ID], Chris Watson[2] [ID], Sophie Maguire[1], Andrew J. Kavanagh[7] [ID], Shun-Rong Zhang[3] [ID], Larisa Goncharenko[3] [ID], Asti Bhatt[8] [ID], Gareth Dorrian[1] [ID], Keith Groves[9] [ID], Alan G. Wood[1] [ID], and Ben Reid[1,2]

[1]Space Environment and Radio Engineering Group (SERENE), School of Engineering, University of Birmingham, Birmingham, UK, [2]Department of Physics, University of New Brunswick, Fredericton, NB, Canada, [3]Haystack Observatory, Massachusetts Institute of Technology, Tyngsborough, MA, USA, [4]Department of Atmospheric and Oceanic Sciences, University of California Los Angeles, Los Angeles, CA, USA, [5]Department of Physics and Applied Physics, University of Massachusetts, Lowell, MA, USA, [6]Center for Solar-Terrestrial Research, New Jersey Institute of Technology, Newark, NJ, USA, [7]British Antarctic Survey, Cambridge, UK, [8]SRI International, Menlo Park, CA, USA, [9]Boston College, Chestnut Hill, MA, USA

Abstract The high latitude ionospheric evolution of the May 10-11, 2024, geomagnetic storm is investigated in terms of Total Electron Content and contextualized with Incoherent Scatter Radar and ionosonde observations. Substantial plasma lifting is observed within the initial Storm Enhanced Density plume with ionospheric peak heights increasing by 150–300 km, reaching levels of up to 630 km. Scintillation is observed within the cusp during the initial expansion phase of the storm, spreading across the auroral oval thereafter. Patch transport into the polar cap produces broad regions of scintillation that are rapidly cleared from the region after a strong Interplanetary Magnetic Field reversal at 2230UT. Strong heating and composition changes result in the complete absence of the F2-layer on the eleventh, suffocating high latitude convection from dense plasma necessary for Tongue of Ionization and patch formation, ultimately resulting in a suppression of polar cap scintillation on the eleventh.

Plain Language Summary The intense geomagnetic storm of May 2024 caused a plethora of different responses within the Earth's ionosphere. In the early phases of the storm, the auroral oval quickly expands to upper midlatitudes and induces strong variations in Global Navigation Satellite System (GNSS) phase measurements. Concurrently, midlatitude plasma is repeatedly lifted by 100–300 km on timescales of about an hour resulting in enhanced plasma densities. This intensified and lifted plasma is then drawn into the polar cap inducing variations in GNSS amplitude and phase. As the storm evolves, heating drives mixing of the thermosphere and causes an extreme depletion in ionospheric plasma. After 24 hr, despite severe geomagnetic conditions persisting, the depleted plasma environment results in only relatively weak plasma transport into the polar cap and significantly reduced impacts on GNSS.

1. Introduction

The May 10-11, 2024, geomagnetic storm was the first Kp 9 storm since 2003 and had sustained geomagnetic activity levels greater than Kp 8 for at least 24 hr. The storm was a 1-in-12.5 [11.3, 13.6] year storm in terms of intensity but was a 1-in- 41 [27,67] year storm in terms of duration (Elvidge & Themens, 2024). This prolonged period of intense geomagnetic activity allows us to examine how prior geomagnetic activity might affect the ionospheric response to prolonged intense geomagnetic storms and its subsequent impact on communications and navigation systems.

Figures 1b and 1c present the solar wind Interplanetary Magnetic Field (IMF), flow speed, and plasma density, shifted in time for L1-magnetopause propagation and in GSM coordinates. The Dst and Kp geomagnetic indices for this period are plotted in Figure 1a. We note perturbed solar wind magnetic field variations beginning at ~1700UT with corresponding sudden commencement behavior coincidently observed in Dst. Subsequent geomagnetic activity peaks in Dst at 02UT on May 11th at −412 nT, while Kp peaks at 9 for 00UT and 09UT. Higher temporal resolution Kp-like geomagnetic indices, which are not capped at 9, have been investigated in Yamazaki et al. (2024) but will not be presented here. In terms of IMF, particularly notable features are the largest
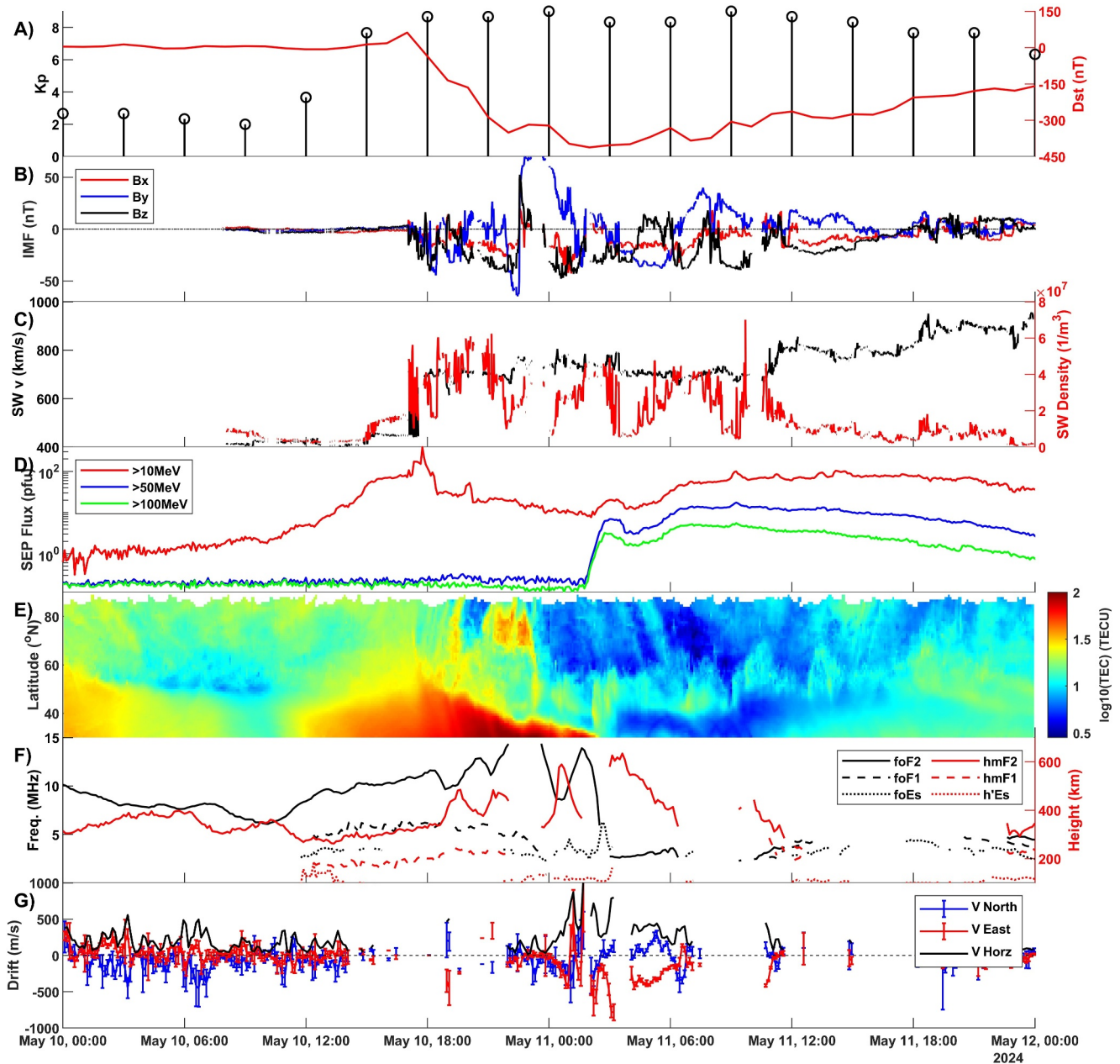
Figure 1. (a) Kp Index (black) and Dst (red) for the May 10–11, 2024 period. (b) Corresponding OMNI-shifted IMF Bx (red), By (blue), and Bz (black) in GSM coordinates. (c) Solar Wind speed (black) and solar wind density (red). (d) SEP fluxes for >10 MeV (red), >50 MeV (blue), and >100 MeV (green) particle energies. (e) Meridional cross section of zonally averaged TEC between 90°W and 80°W, corresponding to a ±5° longitude band around the Eglin Air Force Base (AFB) ionosonde. (f) Peak critical frequency (black) and height (red) of the F2 (solid), F1 (dashed), and Sporadic-E (dotted) layers at the Eglin AFB ionosonde. (g) Magnetic North-South (blue) and East-West (red) F-Region plasma drift at the Eglin AFB ionosonde, with the horizontal drift magnitude in black.

excursions in Bz reaching −40.4, −43.4, −47.9, −38.7, and −39.6 nT at 1807UT (tenth), 2212UT (tenth), 0036UT (eleventh), 0607UT (eleventh), and 0928UT (eleventh), respectively, and the substantial 132.7 nT shift in IMF By beginning at 2230UT and stabilizing at 2248UT on May 10th.

Coincident with this period of heightened geomagnetic activity is a pair of Solar Energetic Proton events (SEPs). The first event had modest SEP >10 MeV fluxes exceeding 10 pfu at 1330UT on May 10th. A second event with larger high-energy particle fluxes arrived on May 11th, with fluxes beginning to increase at ∼0200UT and eventually peaking ∼0700UT. The SEP conditions for this event, as measured on the primary Geostationary Operational Environmental Satellite (GOES), is presented in Figure 1d. The coincidence of this SEP event with

the geomagnetic storm poses some substantial challenges for studying the event, as increased polar cap absorption resulted in virtually complete blackout conditions across the High Frequency (HF) radio band for much of the event, particularly after the arrival of the second SEP with higher high energy particle fluxes. This substantially limits the availability of HF-dependent remote sensing systems, like SuperDARN and ionosondes. The availability of the HF band at a number of locations is provided in the Supporting Information S1.

Sojka et al. (1994) show, both through modeling and topside in situ measurements, that the changes in thermospheric composition and strong outflow during periods of sustained very-high geomagnetic activity associated with the March 1989 storm result in a considerably expanded polar ionospheric hole and substantially lower plasma densities at midlatitudes, subsequently resulting in weaker Tongue of Ionization (ToI) formation. In this study, we further explore this in the context of the May 2024 storm and furthermore examine the subsequent impacts on Global Navigation Satellite Systems (GNSS) and HF propagation. By comparing the response to geomagnetic activity in earlier phases of the storm to periods of similar activity 24 hr later, we demonstrate the effects of intense geomagnetic preconditioning of the Ionosphere-Thermosphere (IT) and its impacts on subsequent geomagnetic activity responses of the IT system, while also providing an overview of the general ionospheric response to the May 2024 geomagnetic storm.

2. Observations

In this study we use measurements from a broad range of instruments to diagnose the high latitude ionospheric response to the May 2024 storm, including GNSS receivers, ionosondes, and Incoherent Scatter Radars (ISRs). In particular, substantial use is made of the Massachusetts Institute of Technology (MIT) Madrigal database of GNSS Total Electron Content (TEC) and scintillation data (Rideout & Coster, 2006; Vierinen et al., 2016). Data from Madrigal is acquired as $1° \times 1°$ degree, 5-min temporal resolution maps for TEC and as scintillation indices (S4 and σ_{Phi}). For the purposes of this study, a 30° elevation cutoff was applied to the scintillation observations to remove some of the influence of multipath. The thin shell altitude used to calculate the Ionospheric Pierce Point (IPP) for the scintillation observations was taken as 350 km. It should be noted that much of the scintillation that we see in this study was most likely the result of structures in the E-Region; as such, the geolocation of structures in the maps presented in Figures 2–4 is approximate, with an uncertainty of up to 150 km at the lowest elevations. Maps of vertical TEC (vTEC) and superimposed phase (circles) and amplitude (x's) scintillation indices are presented in Figure 2 for the initial auroral expansion (~1700UT to 2200UT on May 10th), in Figure 3 for the evolution of plasma patches (~2200UT to 0000UT at the end of May 10th), and in Figure 4 for the subsequent evolution of the storm, including several periods 24 hr after those observed in Figures 2 and 3. We have saturated the color scale of these maps at 45TECU to better highlight the structure at high latitudes. The thin shell projection used in mapping TEC may result in errors in structure geolocation and some smoothing of sharp gradients, but this should not affect the qualitative examination herein. Scintillation indices are plotted in these maps only if they exceed 0.15, where the size of the plotted symbol corresponds to the scintillation intensity above this threshold for qualitative comparison. A video of the overall evolution of the storm in terms of TEC and scintillation is provided in the Supporting Information S1.

Ionosonde observations of bottomside electron density are gathered from the Global Ionospheric Radio Observatory (GIRO) (B. W. Reinisch and Galkin, 2011) for the Eglin ionosonde (30.50°N, 273.50°E) and were manually processed (scaled) to measure precise ionospheric peak critical frequencies and layer heights, plotted in Figure 1f. F-Region plasma drift observations (Reinisch et al., 1998; Kouba & Knížová, 2012) from this ionosonde are also used and presented in Figure 1g.

Finally, observations from the 42m dish of the European Incoherent Scatter Radar (EISCAT) Svalbard Radar (ESR; 78.09°N, 16.02°E) (Wannberg et al., 1997) and the Long Pulse (LP) field-aligned beam of the Poker Flat Incoherent Scatter Radar (PFISR; 65.13°N, 212.53°E) (Heinselman & Nicolls, 2008) are also used to examine the vertical structure of plasma patches, particle precipitation, and long term compositional effects on the F-Region ionosphere. Data from these ISRs are plotted in Figure 5. During this period, the 42m dish of ESR was operated in a near-vertical, field-aligned configuration in its International Polar Year (IPY) mode, while PFISR operated a varying series of modes, including their IPY27, MSWinds, THEMIS36, and LLITED modes, all of which have a field-aligned beam. Observations from ISRs are particularly critical for understanding this event, as the coincident SEP and substantial expansion of the auroral oval, and thus rigidity cutoff boundary, resulted in most ionosondes experiencing debilitating absorption throughout much of this event. An illustration of the attenuation experienced
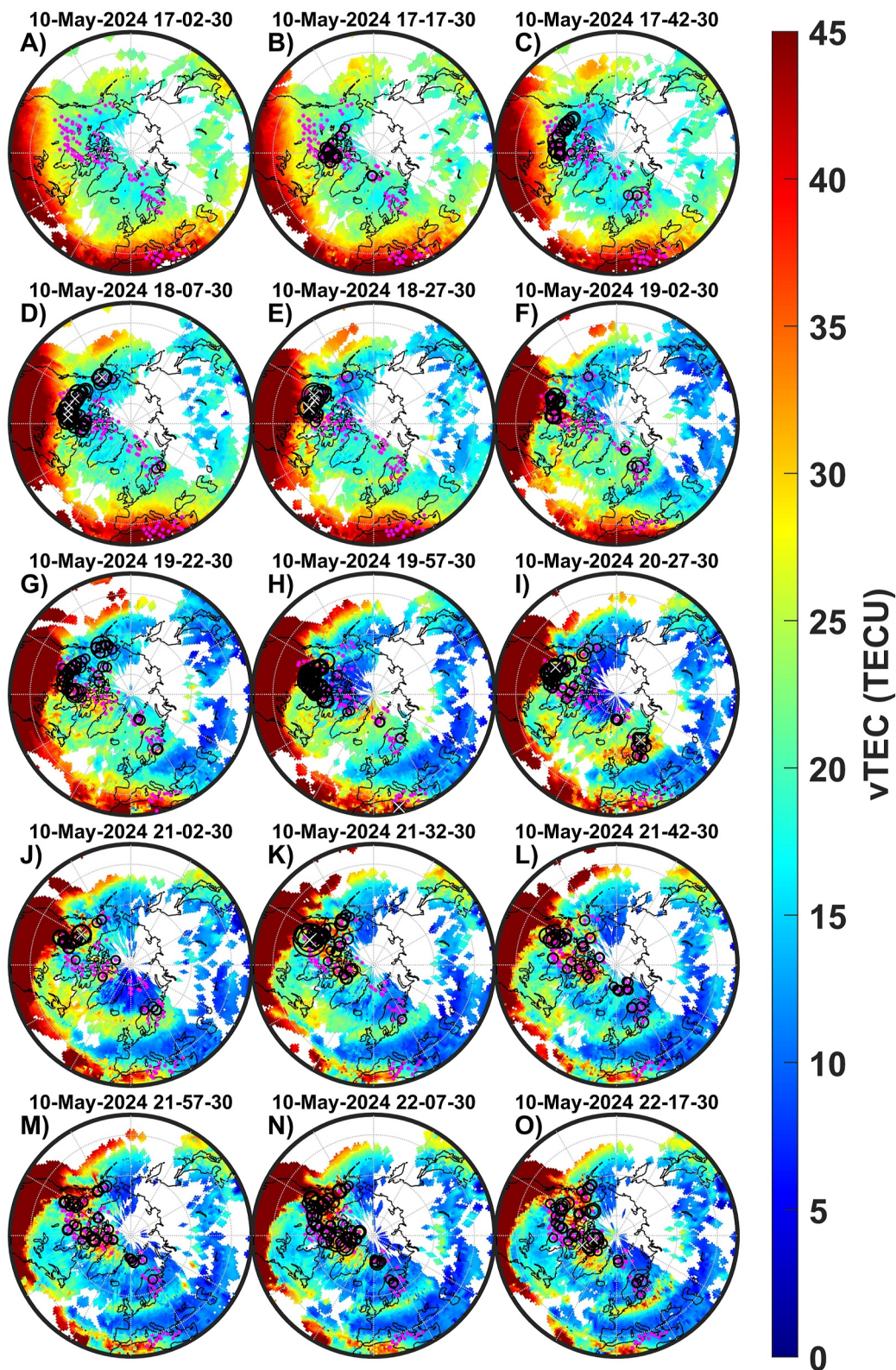
Figure 2. Snapshots of the evolution of TEC (contours), S4 (x's), and σ_{Phi} (o's) over the initial development phase of the storm between 1700UT and 2217UT. Magenta dots represent the location of the scintillation observation IPPs.

Figure 3. Snapshots of the evolution of TEC (contours), S4 (x's), and σ_{Phi} (o's) during the strong shift in IMF orientation beginning at 2230UT and spanning until 2342UT.
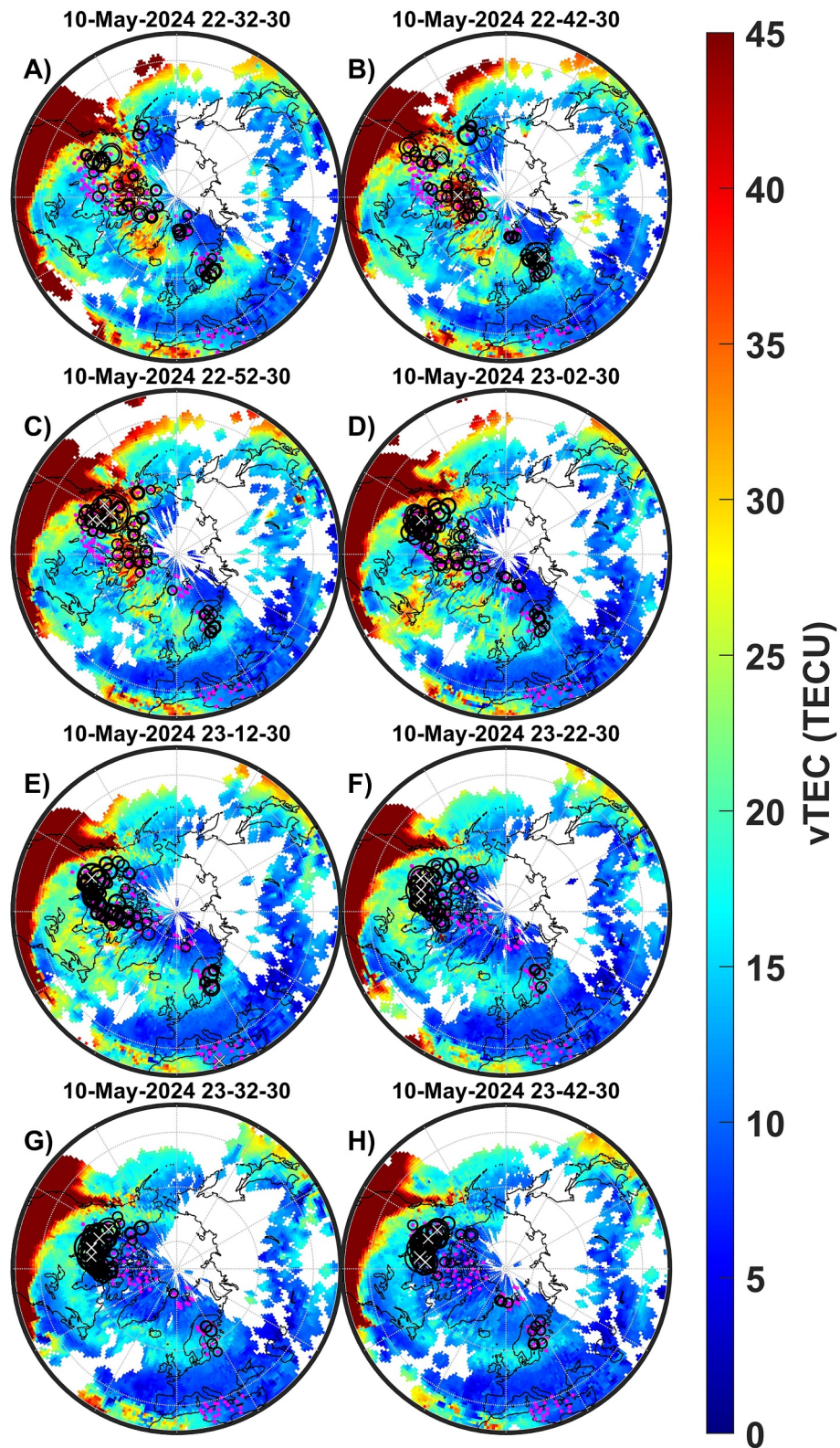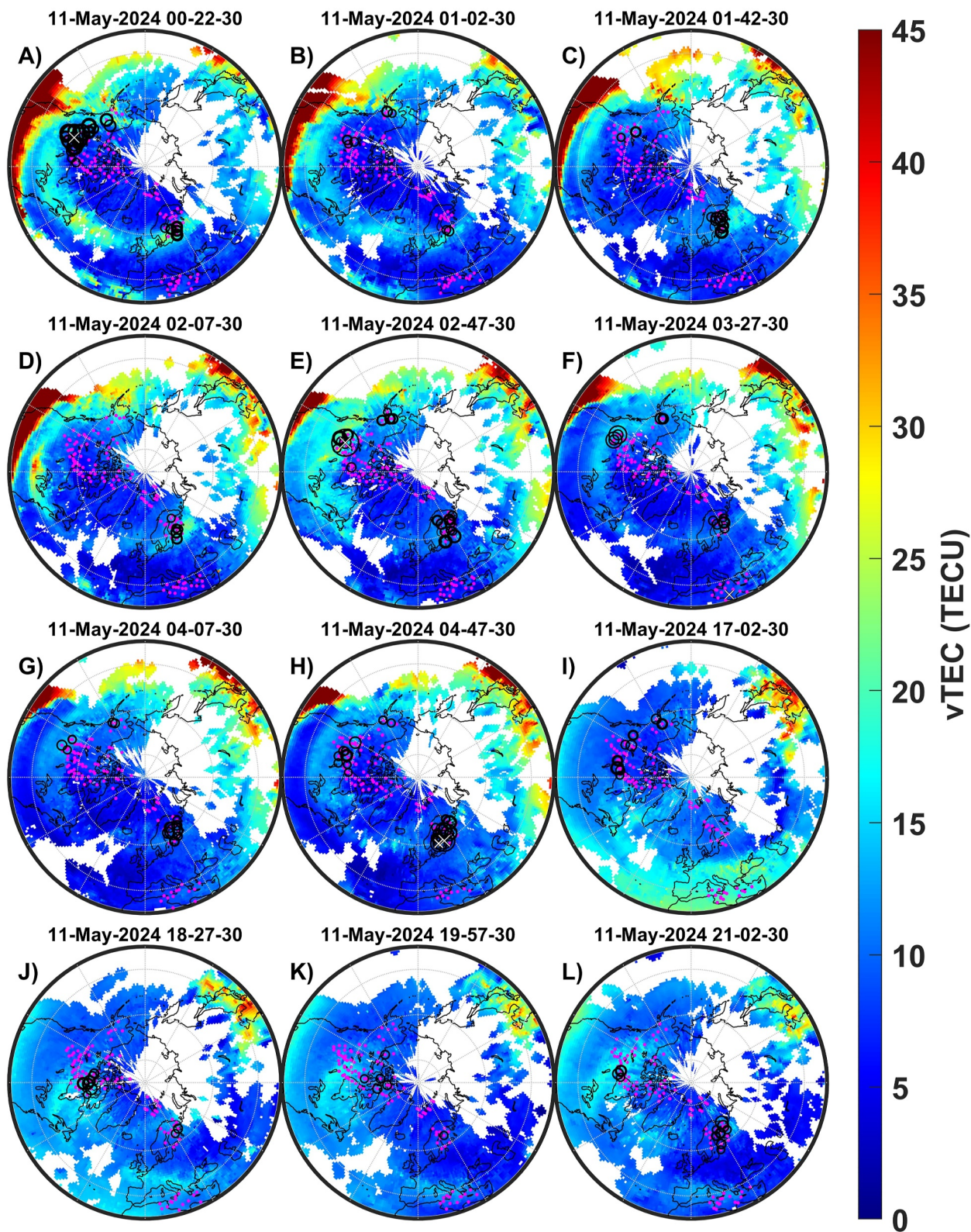
Figure 4. Example snapshots of the evolution of TEC (contours), S4 (x's), and σ_{Phi} (o's) during the remaining evolution of the geomagnetic storm after 2230UT on May 10th until 2102UT on May 11th.
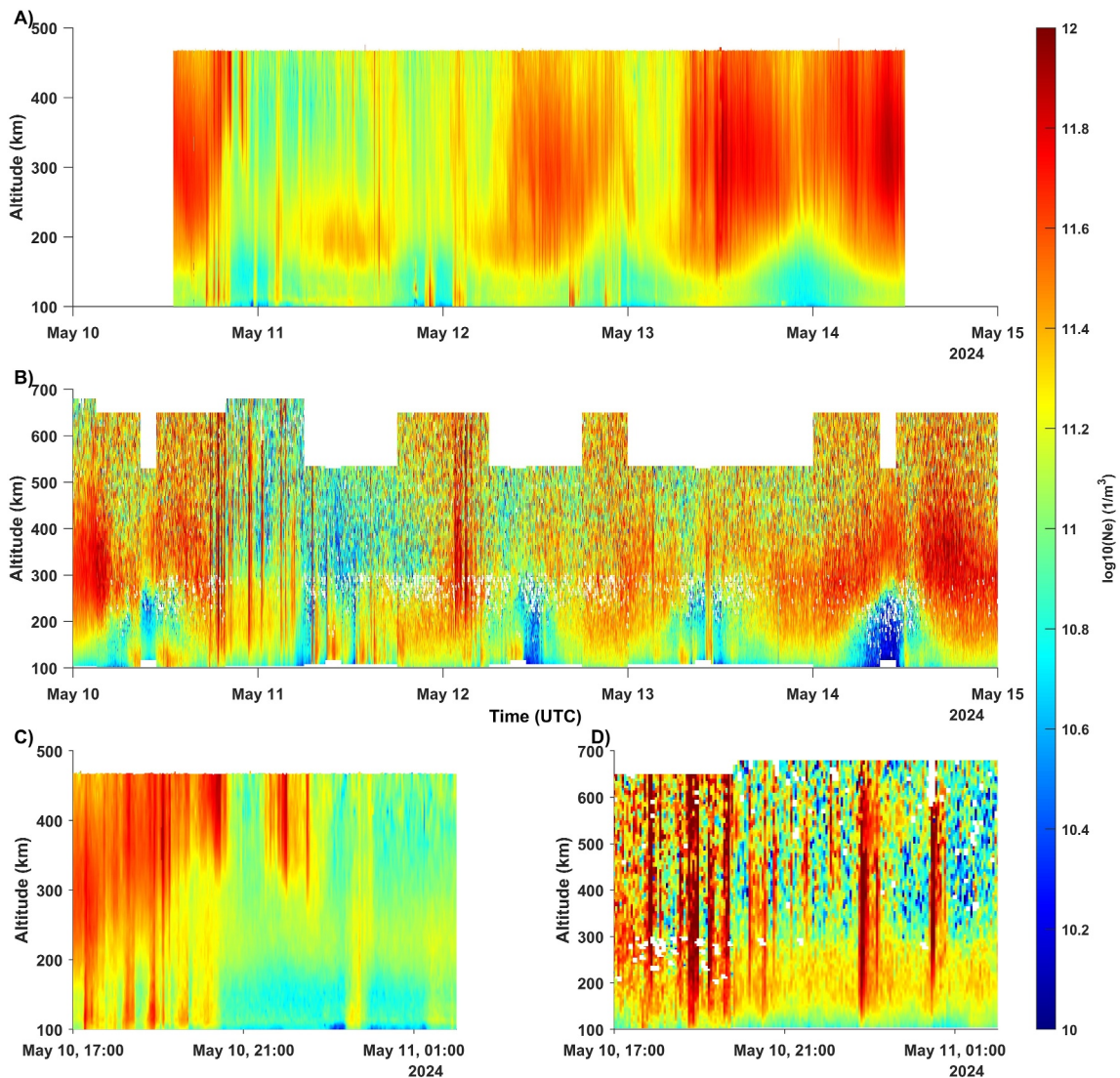
Figure 5. (a) Vertical logarithmic electron density contours at ESR between May 10th and 14 May 2024. (b) same as (a) but for PFISR. c/d) Zoomed in electron density at ESR (c) and PFISR (d) between 1700UT on May 10th and 0200UT on May 11th.

by ionosondes at various latitudes is provided in the Supporting Information S1 but will otherwise not be the focus of this study.

3. Results and Discussion

In Figure 2, we see the initial evolution of the ionospheric response to the geomagnetic storm. Shortly after 1700UT, we see a dramatic expansion of the auroral oval, seen clearly as a narrow ring-like band at ~60°N geomagnetic latitude in Figure 2e, clearest in TEC over Scandinavia and Alaska. During this expansion, enhanced σ_{Phi} phase variations were observed to propagate southward in or near the cusp over Northern Canada and later Alaska, with no corresponding scintillation activity over Norway (despite observational availability) until a substorm expansion occurs after 2000 UT. In Figure 5, at ~1800UT at PFISR, this expanded auroral structure corresponds to enhanced electron densities in the lower E-Region, likely the result of medium or high energy particle precipitation (Figure 5d). Unfortunately, the anomalously large enhancement in topside electron densities only in the field-aligned beam suggest that the beam is significantly corrupted by Naturally Enhanced Ion Acoustic Lines (NEIALs) (Akbari & Semeter, 2014). These anomalous structures coincide with the onset of phase and amplitude scintillation over Alaska.

Shortly after this auroral expansion, a small Storm-Enhanced Density (SED) plume (Kelley et al., 2004) develops after 1830UT, forming a patch that reaches ESR at 2000UT, with only intermittent associated phase variation activity. At ESR (Figure 5c), we see plasma with peak heights in excess of the ESR maximum altitude of 475 km. Upon reaching ESR, the patch appears to enter a region of particle precipitation, seen in the TEC observations (Figures 2g–2i) and in the ESR observations as enhanced E-Region density ahead of the patch arrival. Shortly after passing ESR, this patch enters a westward auroral surge and appears to dissipate.

Following this initial development phase of the ionospheric response to the geomagnetic storm, substorm activity begins and a pronounced ToI rapidly develops after 2100UT, with significant subsequent patch formation (Figures 2j–2o). At 2230UT (Figure 3a), PFISR enters the end of the SED plume. At this time, in Figure 5d we see enhanced plasma densities at PFISR and a significantly extended F-Region that is present in most beams but could still be an artifact. A first set of patches (Figures 2l–2o), reach ESR by 2140UT and can be tracked continuously in the TEC observations from their creation. In Figure 5c, we see these patches in the ESR observations, where the peak height of the patches again exceeds the 475 km altitude limit of the radar observation mode. It should be noted that these patches appear to be of midlatitude origin splitting off of the SED plume, where plasma was already substantially lifted.

With extensive patch activity throughout the polar cap, phase variations and intermittent amplitude scintillation pervades much of the North American high latitude sector. By 2200UT, IMF Bz has been strongly negative for several hours reaching as low as −43.4 nT and the auroral oval has further extended to 55°N geomagnetic latitude, now encompassing the United Kingdom. An example of the Rate Of TEC Index (ROTI) and loss of lock distribution over the UK during this period is provided as a video in the Supporting Information S1.

At 2230UT, IMF Bz and By swing positive by 90 and 133 nT, respectively. ∼30 min after this shift in IMF conditions, the substantial patch activity throughout the polar cap is rapidly cleared to the south toward the Atlantic Ocean over the course of ∼1 hr (Figure 3), leaving the polar cap largely devoid of patches thereafter. The ∼30 min delay before the substantial changes in patch motion begin is consistent with climatological delay in the ionospheric response to By reversals observed by Case et al. (2020). Following this exodus of patches from the polar cap, GNSS phase variations are largely isolated to the poleward boundary of the auroral oval for the remainder of the storm, illustrated in example snapshots in Figure 4, with the full time series available in Movies S1 and S2. Patches and ToIs are either too weak to cause substantial subsequent scintillation or simply do not form in the subsequent 24 hr.

Similar to the modeling by Sojka et al. (1994) for the March 1989 storm, substantial ion outflow and thermospheric heating are likely prevalent throughout the initial phase of this storm. As observed by Evans et al. (2024), the O/N$_2$ ratio during this storm decreased by 50% across all but the equatorial anomaly region after the first few hours of the storm and thermospheric temperatures increased by 50%. These factors result in a severe depletion of electron density not only in the polar cap, but also well into relatively low mid latitude regions, such as seen in the Mediterranean region during this event in Spogli et al. (2024). This is highlighted here in the storm response at Eglin, a decidedly midlatitude ionosonde location.

During the initial phase of the storm at Eglin, the peak height of the ionosphere (hmF2) rises quickly by ∼150 km as it resides within the strong SED region. In Figure 1f, the height and peak critical frequency of the F2 peak (foF2) exhibit Large Scale Traveling Ionospheric Disturbance (LSTID)-like oscillations with a period of ∼2 hr, an hmF2 variation amplitude ranging from 150 to 300 km, and an foF2 variation amplitude of ∼2 MHz, comparable to the variation amplitudes seen in Japan during the Halloween Storm (Abdu et al., 2007). Both of these variations ultimately modulate an overall lifting and enhancement of the F-Region plasma at Eglin culminating in hmF2 reaching as high as 630 km and foF2 exceeding the upper frequency limit of the ionosonde such that foF2 likely significantly exceeded 15 MHz. Between 0200UT and 0300UT, Eglin transitions across the edge of the SED region and peak electron density drops by a factor of 20, seen in the foF2 in Figure 1f and in TEC at Eglin's location, nearly on top of the *x*-axis, in Figure 1e. Coincident with this gradient at the edge of the SED region is a strong, thin, well defined Sporadic-E layer, shown as dotted lines in Figure 1f. While Sporadic-E does occur intermittently at this time of day at Eglin, the intensity of the Sporadic-E during this transition across the SED edge is the highest observed at this time of day within 4 days before or after this storm. An illustration of the relative strength of this Sporadic-E with respect to several days prior and after is provided in the Supporting Information S1. It is likely that this Sporadic-E layer is formed via electric field convergence, most typically seen in the dusk cell of the polar cap convection pattern, but possible at mid-latitudes if a sufficiently strong electric

field is present, as we might expect around Sub-Auroral Polarization Streams (SAPS) (Kirkwood & Nilsson, 2000).

At the edge of the SED region at ~0000UT on May 11, in Figure 1g Eglin F-Region plasma drifts show a period of ~1 hr of strong Southwestward drifts of as much as 460 m/s. At 0100 UT, these drifts quickly shift and intensify to 850 m/s Southeastward for ~20 min before swinging Northwestward at 400 m/s at 0120UT, transitioning to greater than 1000 m/s Northeastward at 0130UT, and swinging Southwestward at 0200UT before stabilizing after 0230UT with dominantly westward drifts of initially 800 m/s at 0300UT, decreasing to 400 m/s by 0400UT. These relatively short drift structures are likely Sub-Auroral Ion Drift (SAID) or Sub-Auroral Polarization Stream (SAPS) flow channels along the edge of the SED region at sunset. These strong drift shears and associated electric fields likely also modulate the formation of the Sporadic-E layer on the edge of the SED region and contribute to the sudden enhancement in Sporadic-E intensity at the edge crossing. Given the role of lower ionospheric conductivity in SAPS dynamics (Foster & Burke, 2002), further investigation of the interaction between these flow channels and the Sporadic-E layer is likely warranted but is outside the scope of this initial study.

Following the passing of the SED region, Eglin F-Region electron density remains significantly depleted throughout the next day, with ionospheric G-Condition, where the F1-layer plasma density exceeds the F2 density, persisting until shortly before sunset on May 11th. The severe depletion of plasma, even at midlatitudes, can also be seen in the TEC keogram in Figure 1e, where the TEC at midlatitudes appears to be at least half an order of magnitude lower on the eleventh compared to pre-storm conditions on the tenth. While, because of G-Condition, the Eglin ionosonde could not provide a full picture of the status of the F region plasma environment on the eleventh and thereafter, observations from ESR and PFISR are not encumbered and provide valuable insight. Examining the vertical ionospheric structure at ESR and PFISR in Figures 5a and 5b, respectively, we see that the F2-Region is largely non-existent, with plasma densities at F2-Region altitudes an entire order of magnitude lower on the eleventh compared to the pre-storm conditions on the tenth. In fact, while the F2-Region recovers on the afternoon of the twelfth, G-Condition structuring of the F-region ionosphere continues to persist at PFISR and ESR before noon on both the twelfth and thirteenth, only recovering to pre-storm morning F region conditions by the morning of the fourteenth.

This extensive depletion of F-Region plasma extending from the polar cap well into lower mid latitudes is likely the direct result of changes in thermospheric composition due to the changes in thermospheric circulation resulting from strong auroral and Joule heating during the storm, as observed for this storm by Evans et al. (2024). At PFISR, the F2-layer disappears almost immediately after the auroral expansion at 1800UT on the tenth. In the absence of F2-Region plasma to transport to high latitudes on the eleventh, the high degree of geomagnetic activity on the tenth has the effect of "suffocating" the still-extensive high latitude convection pattern from the dense plasma needed to form appreciable ToIs and subsequent patches. This furthermore explains the observation of only very minor polar cap σ_{Phi} on the eleventh despite severe geomagnetic disturbance conditions persisting. These results suggest that severe storm duration may not be a significant indicator of impact in terms of GNSS disturbances at high latitudes, at least within the polar cap.

4. Conclusions

We here provide an overview of the evolution of large-scale ionospheric plasma structuring during the May 2024 geomagnetic storm. We track the evolution of scintillation from the initial expansion phase, where scintillation is isolated to the cusp, to the formation of a ToI and patches, to the subsequent severe depletion of mid- and high-latitude plasma density and correspondingly limited generation of significant ToI and patch structures and scintillation on the second day of the event. Lifting of ionospheric plasma at mid-latitudes within the initial SED region over North America saw peak heights reach as high as ~630 km and peak densities several times that of background conditions. The convection of this SED plasma to high latitudes resulted in corresponding plasma patches at ESR and PFISR with peak heights exceeding 400–450 km altitudes.

These results demonstrate the important role of Ionosphere-Thermosphere-Magnetosphere (ITM) coupling in the evolution of large and prolonged geomagnetic disturbances, where the severe depletion of F-Region plasma density in the early phase of the storm results in significantly reduced high-latitude scintillation the subsequent day, despite similarly elevated geomagnetic conditions. Reproduction of this event will thereby require coupled, self-consistent modeling, as the thermospheric response to magnetospheric forcing ultimately strongly influenced the further evolution of the ionosphere. Both accurate magnetospheric forcing to drive thermospheric heating and

high latitude convection, as well as the corresponding thermospheric circulation and composition changes that result in the severe depletion of plasma over high- and mid-latitudes, are essential for reproducing the ionospheric response to this storm and for understanding and predicting the subsequent impacts on technological systems, like GNSS and HF propagation.

As the first Kp 9 storm since the deployment of high-latitude scintillation monitor GNSS networks, like the Canadian High Arctic Ionospheric Network (CHAIN) (Jayachandran et al., 2009), and the availability of high latitude imaging ISRs, like PFISR and the Resolute ISR, this event and the observations herein will be a testbed from which to examine high latitude ITM coupling across scales.

Data Availability Statement

The results presented in this document rely on data provided by provided by the Community Coordinated Modeling Center at Goddard Space Flight Center through their integrated Space Weather Analysis (iSWA) system's HAPI server (https://iswa.gsfc.nasa.gov/IswaSystemWebApp/hapi). The CCMC is a multi-agency partnership between NASA, AFMC, AFOSR, AFRL, AFWA, NOAA, NSF and ONR. The results presented in this document rely on data provided by the GFZ German Research Centre for Geosciences (https://www.gfz-potsdam.de/en/section/geomagnetism/data-products-services/geomagnetic-kp-index). The results presented in this document rely on data produced by the World Data Center (WDC) for Geomagnetism, Kyoto Japan (https://wdc.kugi.kyoto-u.ac.jp/). We acknowledge use of NASA/GSFC's Space Physics Data Facility's OMNIWeb (or CDAWeb or ftp) service, and OMNI data. These four data sets were accessed via the University of Colorado's Space Weather Technology, Research, and Education Center's (https://colorado.edu/spaceweather) Space Weather Data Portal (https://lasp.colorado.edu/space-weather-portal) (University of Colorado Boulder and Space Weather Technology, Research, and Education Center, 2019). The GOES data can be acquired using https://lasp.colorado.edu/space-weather-portal/latis/dap/goess_part_flux_P5M.csv?time,P1,P10,P100,P30,P5,P50&time%3E=2024-05-10T00:00:00Z&time%3C=2024-05-14T00:00:00Z&formatTime(yyyy-MM-dd'T'HH:mm:ss). The Kp data can be acquired using https://lasp.colorado.edu/space-weather-portal/latis/dap/kp.csv?time,enum_index&time%3E=2024-05-10T00:00:00Z&time%3C=2024-05-14T00:00:00Z&formatTime(yyyy-MM-dd'T'HH:mm:ss). The Dst data can be acquired using https://lasp.colorado.edu/space-weather-portal/latis/dap/kyoto_dst_index_service.csv?time,dst&time%3E=2024-05-10T00:00:00Z&time%3C=2024-05-14T00:00:00Z&formatTime(yyyy-MM-dd'T'HH:mm:ss). The OMNI solar wind data can be acquired using https://lasp.colorado.edu/space-weather-portal/latis/dap/omni_hro2_1min.csv?time,BX_GSE,BY_GSE,BZ_GSE,E,Pressure,flow_speed,proton_density,T&time%3E=2024-05-10T00:00:00Z&time%3C=2024-05-14T00:00:00Z&formatTime(yyyy-MM-dd'T'HH:mm:ss). GPS TEC data products and access through the Madrigal distributed data system (Coster, 2024a, 2024b) are provided to the community by the Massachusetts Institute of Technology under support from US National Science Foundation grant AGS-1952737. Data for the TEC processing is provided from the following organizations: UNAVCO, Scripps Orbit and Permanent Array Center, Institut Geographique National, France, International GNSS Service, The Crustal Dynamics Data Information System (CDDIS), National Geodetic Survey, Instituto Brasileiro de Geografia e Estatística, RAMSAC CORS of Instituto Geográfico Nacional de la República Argentina, Arecibo Observatory, Low-Latitude Ionospheric Sensor Network (LISN), Canadian High Arctic Ionospheric Network, Institute of Geology and Geophysics, Chinese Academy of Sciences, China Meteorology Administration, Centro di Ricerche Sismologiche, Système d'Observation du Niveau des Eaux Littorales (SONEL), RENAG: REseau NAtional GNSS permanent (RESIF, 2017), GeoNet - the official source of geological hazard information for New Zealand, Finnish Meteorological Institute, SWEPOS - Sweden, Hartebeesthoek Radio Astronomy Observatory, TrigNet Web Application, South Africa, Australian Space Weather Services, RETE INTEGRATA NAZIONALE GPS, Estonian Land Board, the Canadian High Arctic Ionospheric Network (CHAIN), TU Delft, Western Canada Deformation Array, EUREF Permanent GNSS Network, GeoDAF: Geodetic Data Archiving Facility, African Geodetic Reference Frame (AFREF), Kartverket - Norwegian Mapping Authority, Geoscience Australia, IGS Data Center of Wuhan University, Pacific Northwest Geodetic Array, Nevada Geodetic Laboratory, Earth Observatory of Singapore, National Time and Frequency Standard Laboratory - Taiwan, and Korea Astronomy and Space Science Institute. Scintillation data contributing to the Madrigal Scintillation product (Coster, 2024c, 2024d) are gathered from CHAIN, the Tromso Geophysical Observatory (TGO), the Monitors for Alaskan and Canadian Auroral Weather in Space (MACAWS) network, and the electronic Space Weather upper atmosphere (eSWua)

portal (Cesaroni et al., 2020) managed by the Italian National Institute of Geophysics and Volcanology (INGV), with contributions from the Finnish Meteorological Institute, the Norwegian Mapping Authority, and the Royal Netherlands Meteorological Institute. Incoherent Scatter Radar data for this study was gathered from the CEDAR Madrigal database and are openly available: http://cedar.openmadrigal.org/. Eglin ionosonde manually scaled peak parameters and plasma drifts are available at, along with the ISR data files that were used: https://zenodo.org/doi/10.5281/zenodo.13127184 (Themens et al., 2024).

References

Abdu, M. A., Maruyama, T., Batista, I. S., Saito, S., & Nakamura, M. (2007). Ionospheric responses to the October 2003 superstorm: Longitude/local time effects over equatorial low and middle latitudes. *Journal of Geophysical Research*, *112*(A10), A10306. https://doi.org/10.1029/2006JA012228

Akbari, H., & Semeter, J. L. (2014). Aspect angle dependence of naturally enhanced ion acoustic lines. *Journal of Geophysical Research: Space Physics*, *119*(7), 5909–5917. https://doi.org/10.1002/2014JA019835

Case, N. A., Grocott, A., Fear, R. C., Haaland, S., & Lane, J. H. (2020). Convection in the magnetosphere-ionosphere system: A multimission survey of its response to IMF by reversals. *Journal of Geophysical Research: Space Physics*, *125*(10), e2019JA027541. https://doi.org/10.1029/2019JA027541

Cesaroni, C., De Franceschi, G., Marcocci, C., Pica, E., Romano, V., & Spogli, L. (2020). Electronic Space weather upper atmosphere database (eSWua) - GNSS scintillation data, version 1.0. Istituto Nazionale di Geofisica e Vulcanologia (INGV) August 1. [Dataset]. https://doi.org/10.13127/ESWUA/GNSS

Coster, A. (2024a). Data from the CEDAR madrigal database. Retrieved from https://w3id.org/cedar?experiment_list=experiments4/2024/gps/10may24&file_list=gps240510g.001.hdf5,MIT/HaystackObservatory

Coster, A. (2024b). Data from the CEDAR madrigal database. Retrieved from https://w3id.org/cedar?experiment_list=experiments4/2024/gps/11may24&file_list=gps240511g.001.hdf5,MIT/HaystackObservatory

Coster, A. (2024c). Data from the CEDAR madrigal database. Retrieved from https://w3id.org/cedar?experiment_list=experiments/2024/sci/10may24&file_list=scin_20240510.001.hdf5,MIT/HaystackObservatory

Coster, A. (2024d). Data from the CEDAR madrigal database. Retrieved from https://w3id.org/cedar?experiment_list=experiments/2024/sci/11may24&file_list=scin_20240511.001.hdf5,MIT/HaystackObservatory

Elvidge, S., & Themens, D. R. (2024). *The Probability of the May 2024 Solar Superstorm, 15 August 2024, PREPRINT (Version 1)*. Research Square. https://doi.org/10.21203/rs.3.rs-4780404/v1

Evans, J. S., Correira, J., Lumpe, J. D., Eastes, R. W., Gan, Q., Laskar, F. I., et al. (2024). GOLD observations of the thermospheric response to the 10–12 May 2024 Gannon superstorm. *Geophysical Research Letters*, *51*(16), e2024GL110506. https://doi.org/10.1029/2024GL110506

Foster, J. C., & Burke, W. J. (2002). Saps: A new categorization for sub-auroral electric fields. *Eos Trans. AGU*, *83*(36), 393–394. https://doi.org/10.1029/2002EO000289

Heinselman, C. J., & Nicolls, M. J. (2008). A bayesian approach to electric field and E-region neutral wind estimation with the poker Flat advanced modular incoherent scatter radar. *Radio Science*, *43*(5), RS5013. https://doi.org/10.1029/2007RS003805

Jayachandran, P. T., Langley, R. B., MacDougall, J. W., Mushini, S. C., Pokhotelov, D., Hamza, A. M., et al. (2009). Canadian high arctic ionospheric network (CHAIN). *Radio Science*, *44*(1), RS0A03. https://doi.org/10.1029/2008RS004046

Kelley, M. C., Vlasov, M. N., Foster, J. C., & Coster, A. J. (2004). A quantitative explanation for the phenomenon known as storm-enhanced density. *Geophysical Research Letters*, *31*(19), L19809. https://doi.org/10.1029/2004GL020875

Kirkwood, S., & Nilsson, H. (2000). Nilsson (2000), H. High-Latitude sporadic-E and other thin layers – The role of magnetospheric electric fields. *Space Science Reviews*, *91*(3/4), 579–613. https://doi.org/10.1023/A:1005241931650

Kouba, D., & Knížová, P. K. (2012). Analysis of digisonde drift measurements quality. *Journal of Atmospheric and Solar-Terrestrial Physics*, *90*(91), pp212–221. https://doi.org/10.1016/j.jastp.2012.05.006

Reinisch, B. W., & Galkin, I. A. (2011). Global ionospheric radio observatory (GIRO). *Earth Planets and Space*, *63*(4), 377–381. https://doi.org/10.5047/eps.2011.03.001

Reinisch, B. W., Scali, J. L., & Haines, D. M. (1998). Ionospheric drift measurements with ionosondes. *Annali di Geofisica*, *41*(5–6), 695–702. https://doi.org/10.4401/ag-3812

RESIF. (2017). RESIF-RENAG French national geodetic network. [Dataset]. *RESIF - Réseau Sismologique et géodésique Français*. https://doi.org/10.15778/RESIF.RG

Rideout, W., & Coster, A. (2006). Automated GPS processing for global total electron content data. *GPS Solutions*, *10*(3), 219–228. https://doi.org/10.1007/s10291-006-0029-5

Sojka, J. J., Schunk, R. W., & Denig, W. F. (1994). Ionospheric response to the sustained high geomagnetic activity during the March '89 Great Storm. *Journal of Geophysical Research*, *99*(A11), 21341–21352. https://doi.org/10.1029/94JA01765

Spogli, L., Alberti, T., Bagiacchi, P., Cafarella, L., Cesaroni, C., Cianchini, G., et al. (2024). The effects of the may 2024 mother's day superstorm over the mediterranean sector: From data to public communication. *Annals of Geophysics*, *67*(2), PA218. https://doi.org/10.4401/ag-9117

Themens, D. (2024). The high latitude ionospheric response to the major may 2024 geomagnetic storm: A synoptic view. [Dataset]. *Zenodo*. https://doi.org/10.5281/zenodo.13127185

University of Colorado Boulder and Space Weather Technology, Research, and Education CenterSWx TREC Space Weather Data Portal. (2019). [Dataset]. *Laboratory for Atmospheric and Space Physics*. https://doi.org/10.25980/NMFX-XX89

Vierinen, J., Coster, A. J., Rideout, W. C., Erickson, P. J., & Norberg, J. (2016). Statistical framework for estimating GNSS bias. *Atmospheric Measurement Techniques*, *9*(3), 1303–1312. https://doi.org/10.5194/amt-9-1303-2016

Wannberg, G., Wolf, I., Vanhainen, L., Koskenniemi, K., Röttger, J., Postila, M., et al. (1997). The EISCAT svalbard radar: A case study in modern incoherent scatter radar system design. *Radio Science*, *32*(6), 2283–2307. https://doi.org/10.1029/97RS01803

Yamazaki, Y., Matzka, J., da Silva, M. V. S., Kervalishvili, G. N., & Rauberg, J. (2024). Assessment of Kp=9 geomagnetic storms including the may 2024 "gannon storm" based on version 3.0 hpo indices. *ESS Open Archive*. https://doi.org/10.22541/essoar.171838396.68563140/v2